bradscholars

Constraint-Based Soft Tissue Simulation for Virtual Surgical Training

Item Type	Article
Authors	Tang, W.;Wan, Tao Ruan
Citation	Tang W and Wan TR (2014) Constraint-Based Soft Tissue Simulation for Virtual Surgical Training. IEEE Transactions on Biomedical Engineering. 61(11): 2698-2706
DOI	https://doi.org/10.1109/TBME.2014.2326009
Rights	© 2014 IEEE. Personal use of this material is permitted. Permission from IEEE must be obtained for all other uses, in any current or future media, including reprinting/republishing this material for advertising or promotional purposes, creating new collective works, for resale or redistribution to servers or lists, or reuse of any copyrighted component of this work in other works.
Download date	2025-07-17 03:44:01
Link to Item	http://hdl.handle.net/10454/11302

Constraint-based Soft Tissue Simulation for Virtual Surgical Training

Wen Tang, Tao Ruan Wan *Member, IEEE*

Abstract—Most of surgical simulators employ a linear elastic model to simulate soft tissue material properties due to its computational efficiency and the simplicity. However, soft tissues often have elaborate nonlinear material characteristics. Most prominently soft tissues are soft and compliant to small strains, but after initial deformations they are very resistant to further deformations even under large forces. Such material characteristic is referred as the nonlinear material incompliant which is computationally expensive and numerically difficult to simulate. This paper presents a constraint-based finite element algorithm to simulate the nonlinear incompliant tissue materials efficiently for interactive simulation applications such as virtual surgery. Firstly, the proposed algorithm models the material stiffness behaviour of soft tissues with a set of three-dimensional strain limit constraints on deformation strain tensors. By enforcing a large number of *geometric* constraints to achieve the material stiffness, the algorithm reduces the task of solving stiff equations of motion with a general numerical solver to iteratively resolving a set of constraints with a nonlinear Gauss-Seidel iterative process. Secondly, as a Gauss-Seidel method processing constraints individually, in order to speed up the global convergence of the large constrained system a multi-resolution hierarchy structure is also used to accelerate the computation significantly, making interactive simulations possible at a high level of details. Finally, this paper also presents a simple-to-build data acquisition system to validate simulation results with *ex vivo* tissue measurements. An interactive virtual reality-based simulation system is also demonstrated.

Index Terms—Nonlinear soft tissue simulation and modeling, virtual surgical training, Robotic-assisted surgery.

◆

1 INTRODUCTION

Efficient and accurate simulation of biological soft tissues is a key computational component in virtual reality (VR) based surgical simulators as well as in robotic-assisted surgery and image-guided surgery for intraoperative dynamic guidance [Tang et al, 2012]. Despite the rapid development in computer simulation technologies, achieving accurate soft tissue simulation remains challenging, especially medical applications require fast and accurate computations in order to accommodate user interactions and haptic feedbacks.

Modeling material nonlinearity of biological tissues often involves setting up complex constitutive models to determine deformation behaviors of soft tissues [Ogden, 1997], [Bonet and Wood, 2008]. It is well acknowledged that tuning material parameters for these constitutive models to find approximations to their real-world counterparts is a complex and time-consuming task [Mendis, 1995]. In recent years efforts have been made to model the parametrization of complex biomechanical models as an inverse problem that are solved by optimization. For examples, the estimation of elastic properties of soft tissue is solved as a least squares problem in [Eskandari, et al., 2011], and an evolutionary algorithm is used to estimate the parameters of a complex organ behavior model taking into account

of various real patient data sets in [Vidal et al., 2012]. Previous methods for accelerating nonlinear finite element computations include pre-computing various quantities of a constitutive model [Müller et al., 2001], modal analysis to compute deformations in a reduced subspace [James and Pai, 2002], as well as GPU executions [Taylor et al., 2008] and data-driven approaches [Bickel et al., 2009]. Still, a linear model is mostly used in surgical simulators due to its computational efficiency and simplicity [Chentanez et al., 2009], [Pratt et al., 2010].

The distinctive feature of soft tissues such as skin and relaxed muscles is the so called nonlinear material incompliant, which are easily deformed under small forces, but beyond some *thresholds* soft tissues become very stiff and resistant to large deformations even under large forces [Brouwer et al., 2001]. The stiffness characteristic is due to the macroscopic behavior of the materials that are submissive to small deformations only within some *thresholds*. Such material stiffness determines the nonlinear stress-strain relationship of soft tissues and is the key in capturing physical characteristics of the materials. In this paper ,we propose a constraint-based algorithm to simulate the highly incompliant constitutive regimes of soft tissues through the use of a large number *geometric* constraints to enforce the material stiffness.

Most numerical methods perform poorly for large constraint systems both in terms of system convergency and computational efficiency, because the equations of motion of a large constraint system are infinitely stiff and a small time integration step must be carefully chosen to avoid the numerical instability. Instead of using a general

- W. Tang is with the School of Computing, University of Teesside, Middlesbrough, UK, TS1 3BA.
  E-mail: w.tang@tees.ac.uk
- T. R. Wan is with School of Informatics, University of Bradford, Bradford, UK BD7 1DP.
  E-mail: t.wan@bradford.ac.uk

numerical solver to solve a set of stiff equations of motion, the proposed algorithm employs a Gauss-Seidel type procedure to resolve the constraints iteratively. As Gauss-Seidel methods processing constraints individually, in order to speed up the global convergence of the large constrained system, a multi-resolution hierarchy mesh structure is developed to accelerate the global convergence of the constrained system significantly. The multi-resolution approach enforces constraints at each level of the hierarchy structure with different mesh resolutions, making interactive simulations possible for highly incompliant tissue properties at a higher level of detail. We show a simple-to-build acquisition system to validate the simulation results with *ex vivo* tissue measurements and an interactive virtual reality-based simulation system is also demonstrated.

2 MODELLING OF NONLINEAR SOFT TISSUES

2.1 Principal stretches

Classic approaches try to use various constitutive models to describe the stress-strain relationship to model nonlinear soft tissue behaviors [Ogden, 1997]. Instead, we apply constraints directly on the symmetric strain tensor of each finite element(tetrahedron or triangle) to modify the stress-strain relationship nonlinearly to prevent soft tissues from excessive stretching or compressing. We firstly diagonalize the deformation gradient of each element. The material stiffness is characterized by strain ratios with some *thresholds* along principal directions of deformations. We then apply constraints directly on the symmetric strain tensor of each element.

Most cellular tissues such as livers and skins are treated as isotropic, hyperelastic, and incompressible materials [Fung, 1993], [Humprey, 2003]. The state of soft tissue deformation is defined by the deformation gradient $\mathbf{F}$, which is a 3×3 matrix given by:

$$\mathbf{F}(\mathbf{X}) = \frac{\partial \mathbf{x}}{\partial \mathbf{X}} \qquad (1)$$

where $\mathbf{X}$ is the coordinate of a vertex in the material space and $\mathbf{x}$ is the coordinate in the world space. We compute the singular value decomposition of the deformation gradient on each tetrahedral element $\mathbf{F} = \mathbf{U}\hat{\mathbf{\Sigma}}\mathbf{V}^T$, where $\mathbf{U}$ and $\mathbf{V}$ are orthonormal matrices and $\hat{\mathbf{\Sigma}}$ is a nonnegative diagonal matrix expressed by:

$$\hat{\mathbf{\Sigma}} = diag\{\lambda_1, \lambda_2, \lambda_3\} \qquad (2)$$

The nonnegative diagonal entries $\lambda_1, \lambda_2,$ and λ_3 are eigenvalues representing ratios of stretch and compression in the three principal directions invariant to rigid transformations. Using eigenvalues of principle strain to model soft tissue material is not new in biomedical engineering, for example, in the case of uniaxial deformations, the deformation gradient is modeled as a diagonal tensor given by [Holzapfel, 2004]: $\hat{\mathbf{\Sigma}} =$

$diag\{\lambda, \lambda^{-\frac{1}{2}}, \lambda^{-\frac{1}{2}}\}$, where λ is the (applied) stretch in the principal directions. We employ the modified Neo-Hookean material using an energy density function defined by [Bonet and Wood, 2008]:

$$W = \frac{\mu}{2}(I_1 - 3) - \mu \log J + \frac{\beta}{2}(\log J)^2 \qquad (3)$$

where $\mu = \frac{E}{2(1+\nu)}$ and $\beta = \frac{E\nu}{(1+\nu)(1-2\nu)}$ are the Lamé coefficients with E being the Young's modulus and ν being the Poisson ratio. Estimation of the elasticity parameters of E and ν is described in §4.1. The three principal invariants are expressed as $I_1 = \lambda_1^2 + \lambda_2^2 + \lambda_3^2, I_2 = \lambda_1^4 + \lambda_2^4 + \lambda_3^4$ and $I_3 = \lambda_1^2 \lambda_2^2 \lambda_3^2$. In Eq.3, $J = \sqrt{I_3}$. We then analytically differentiate energy Eq. 3 with respect to the invariants to compute forces. Therefore, for stress defined by a strain energy density function, it can be shown that the diagonal matrix $\hat{\mathbf{\Sigma}}$ yields a diagonal stress that is invariant under the rotation of the material space [Bonet and Wood, 2008].

$$\mathbf{P}(\hat{\mathbf{\Sigma}}) = diag(\frac{\partial W}{\partial \lambda_1}, \frac{\partial W}{\partial \lambda_2}, \frac{\partial W}{\partial \lambda_3}) \qquad (4)$$

Once we have calculated the stress $\mathbf{P}(\mathbf{F})$, the force on a tetrahedral vertex can be found by multiplying $\mathbf{P}(\mathbf{F})$ with an area-weighted normal of the tetrahedron [Irving et al., 2006]. Furthermore, we implement a multi-threading algorithm to parallel compute the SVD procedures on tetrahedron elements on Eq.2 to improve the computational time significantly, since SVD is a costly computation (see §4.2 for details).

2.2 Strain limiting constraints

Equation (4) revels that the elastic energy is a function of the singular values $\lambda_1, \lambda_2, \lambda_3$ of the deformation gradient, which are stretches and compressions corresponding to the scaling in the orthogonal principal strain directions. Our constraint-based algorithm enforces the three-dimensional orthogonal scaling constraints on the principal strains by clamping the principal stretch ratios at defined maximum and minimum values, resulting λ^{max} and λ^{min} for isotropic scaling. For example, $\lambda^{max} = 1.25$ and $\lambda^{min} = 0.75$ specify the maximum of 25 percent of stretching and compressing along the principal strain directions, preventing a tetrahedron from undergoing large deformations. This leads to three clamped principal strains defined by:

$$\begin{aligned}
\lambda_1^* &= clamp(\lambda_1, \ \lambda_1^{min}, \ \lambda_1^{max}), \\
\lambda_2^* &= clamp(\lambda_2, \ \lambda_2^{min}, \ \lambda_2^{max}), \\
\lambda_3^* &= clamp(\lambda_3, \ \lambda_3^{min}, \ \lambda_3^{max}).
\end{aligned} \qquad (5)$$

Thus, a new diagonal strain matrix is constructed based on the constrained values as: $\hat{\mathbf{\Sigma}}^* = diag\{\lambda_1^*, \lambda_2^*, \lambda_3^*\}$. Substituting $\hat{\mathbf{\Sigma}}^*$ into Eq.4 yields a new constrained stress tensor:
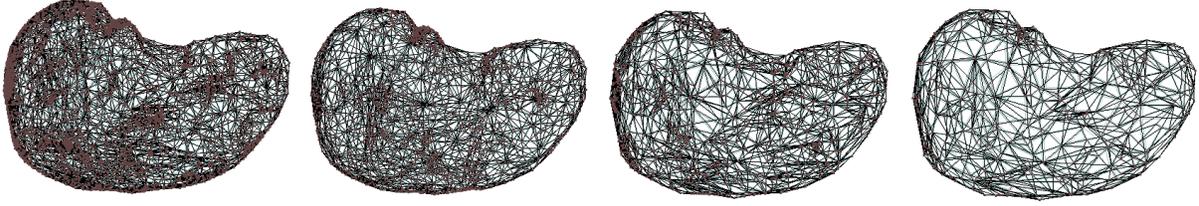
Fig. 1. The multi-resolution hierarchy: A base surface mesh of a liver is extracted from a MRI data set and a fine to coarse hierachy of tetrahedral meshes is generated from the base mesh, containing 17.1K, 15.3K, 0.6K and 0.23K tetrahedra at each level, respectively.

$$\mathbf{P}(\hat{\mathbf{\Sigma}}^*) = diag(\frac{\partial W}{\partial \lambda_1^*}, \frac{\partial W}{\partial \lambda_2^*}, \frac{\partial W}{\partial \lambda_3^*}) \qquad (6)$$

Thus, deformation forces on tetrahedron nodes are re-computed based on the constrained Eq.6. The presence of constrains in the principal directions is clamping the stress at some maximum values and modifying the constitutive model near the origin to remove the singularity, which regularizes the system and enables dynamic simulations remain stable even for deformable objects that simultaneously undergo both free-flying rigid motion and deformations. More importantly, these modifications can be applied to arbitrary constitutive models and our experimental setup is aimed at validating the algorithm to be as accurate as possible for medical simulations.

2.3 Multi-resolution constraint enforcement

The proposed strain limiting algorithm reduces a global solution approach of using the classic method of solving stiff equations of motion to a set of Gauss-Seidel iterations. Because a Gauss-Seidel type solver enforces constraints individually, it can be slow to convergence for a system with a large number of constraints. Taking the view that a hierarchical constraint enforcement can greatly accelerate the system convergence [Müller, 2008], we construct a multi-level hierarchical structure using different tetrahedral mesh resolutions at multi-levels and each level of the hierarchy is solved by a Gauss-Seidel iterative process. Therefore, our multi-resolution approach enforces unilateral constraints from fine meshes to coarser meshes, and then translate the solutions of coarser meshes back to finer levels. This process is termed as up- and down-sampling processes. Figure 2 shows the geometric correspondence between elements in a tetrahedral hierarchy.

The multi-resolution hierarchy process starts with the physically-based computation on the bases mesh. Information of the base mesh is down-sampled to carry out the simulation on coarse meshes. At each coarser mesh level, nonlinear Gauss-Seidel iterations are run to enforce limiting constraints on the current coarser level. Results of the nonlinear stain limiting algorithm are then up-sampled on finer level up the hierarchical chain to enforce constraints on the base mesh. We obtained a MRI data set of a liver from our local hospital with ethic
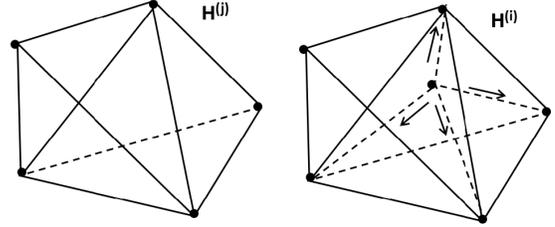

Fig. 2. Geometric correspondence between elements in a tetrahedral hierarchy: solid lines are a coarse mesh $H^{(j)}$ containing a subset of higher resolution meshes $H^{(i)}$ with barycentric coordinates highlighted in dotted red lines.
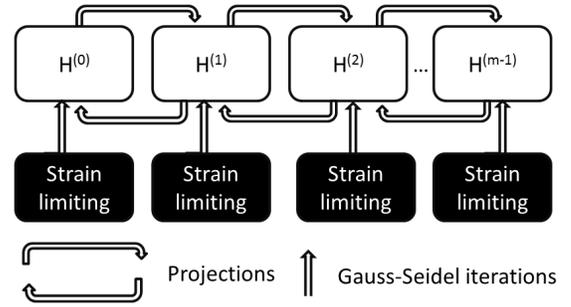

Fig. 3. Multi-resolution mesh hierarchy process pipeline for our simulation system.

clearance approved by our organizations. Segmentation process was carried out manually in the medical image open source software GIMIAS [Gimas] to obtain a base surface mesh of the liver. We then created a hierarchy of surface meshes using the base mesh. TetGen [Si, 2010] was used to convert surface meshes into tetrahedral meshes, containing m levels of meshes $H^{(i)}$, for $i = 0, m-1$, from the finest base level $H^{(0)}$ to the coarsest level of mesh $H^{(m-1)}$ (see figure 1).

For every tetrahedron in a coarser mesh $H^{(j)}$, all vertices of a finer mesh $H^{(i)}$ inside this tetrahedron are determined. For each vertex in $H^{(i)}$ its closest element in $H(j)$ and its corresponding barycentric coordinates are computed. The coordinates are used as interpolation weights for sampling a scalar or a vector field defined over the coarser mesh to the finer mesh using linear interpolation. Mapping values from the finer mesh to the coarse mesh is done using these same weights. The multi-resolution mesh hierarchy process pipeline is summarized in figure 3. The method described here can be divided into a number of stages of computations:

- Dynamic simulation and enforce constraints;
- Downsampling projections;
- Strain limiting on coarse meshes;
- Enforce constraints;
- Upsampling strain limited results.

Given an initial displacement values on the fine mesh we perform the multi-resolution algorithm on the hierarchical data structure:

- Sample positions on the finest level $H^{(0)}$ to obtain $\mathbf{p_i}$ on the coarsest level $H^{(m-1)}$:
- loop:
- Start at the coarsest level:$H^{(i)} \leftarrow H^{(m-1)}$
- Save all positions $\mathbf{p_i}$ of level $H^{(i)}$ in a state vector $\mathbf{q_i}$.
- Run linear Gauss-Seidel iterations to enforce strain limiting constraints.
- If $H^{(i)} = 0$ stop else go to the next finer level:$H^{(i)} \leftarrow H^{(i-1)}$:
- Sample positions on level $H^{(i)}$
- end loop.

Colour maps in figure 4 show strain distributions of a soft tissue simulation. In these images, strain values are scaled to between [0, 1], where value 0 representing the green colour shows the zero strain of the deformation and value 1 representing the red colour indicates the largest strain of the deformation. Images (A) and (B) compare the convergency of the constraint enforcements between a multi-resolution hierarchy approach to that of using only a single mesh with the same finest level mesh resolution. As can be seen that the multi-resolution algorithm archives better strain convergency with only 20 constraint iterations in total, whereas the fine only single mesh simulation shows larger strains after 50 constraint iterations. This test illustrates the effectiveness of the proposed multi-resolution algorithm for modelling highly incompliant soft tissue materials. The strain distributions across different levels of a three-levels mesh hierarchy are shown in images (C), (D) and (E) with 5 iterations on each level.

3 DATA ACQUISITION

We developed a simple-to-build data acquisition system for capturing soft tissue deformations *ex vivo*, which was used to record the indentation and stretch tests on *ex vivo* samples. Simulation results were validated against results obtained by these tests. While *in vivo* experiments can measure soft tissue behaviors in its physiological state [Samur et al., 2007], *ex vivo* tests, however, offer good controls over laboratory experimental conditions [Brouwer et al., 2001].

3.1 Experimental setup

For indentation tests, the force measurement was obtained by a force contact prob (a long thin solid shaft of different tip shapes). A square force sensing resistor of $1.5inch \times 1.5inch$ was attached to the prob tip for measuring tissue force responses. Figure 5 shows schematics of the system. The force sensor was connected to a Phidget Voltage Divider and a USB Interface Kit
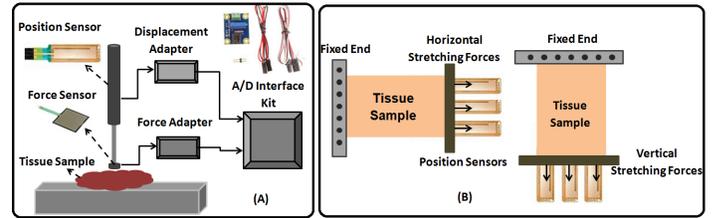

Fig. 5. (A): Overview of the data acquisition system and its components: the force probe was inserted into the trocar cover that was fitted with a linear position sensor. The force sensor was attached to the tip of the probe and A/D interface kit was connected to a computer on Windows operating system, and the force-displacement measurement was taken from *ex vivo* tissue samples. (B): Stretching experiment setup.

8/8/8 by Trossen Robotics for A/D converting controlled from Windows. A force-displacement transducer (linear position sensor) was fitted inside a trocar cover in which the probe was sliding through inside to take the measurement of force-displacement for indentation tests.

Tests were made along a user defined straight path with a constant velocity. The force sensor has the pressure range $[1.5psi,\ 150psi]$ and the actuation force range $[100g,\ 10kg]$ with a repeatable force reading. The linear position sensor had a 6 mm wide active cavity.

The data acquisition system also consisted of a testing board and a pair of slats with one slat fixed on the board and another was free to move vertically and horizontally. The stretching measurements were conducted by using this novel experimental setup, aimed at capturing tissue stretch behaviors by measuring stretch ratios using the biaxial tensile method [Brouwer et al., 2001]. The same force sensor and the linear position sensor were used for a skin sample of size $80mm \times 80mm$ fixed between the two slats on the testing board. Repeated stretching tests were carried out in the two orthogonal stretch directions.

3.2 Experimental procedures

Indentation tests were aimed at validating the force-displacement responses of computer simulation results. These tests also demonstrated tissue relaxation behaviors due to constant and periodic step strains. The stretch tests were aimed at evaluating force-stretch behaviors of the simulated soft tissue.

Porcine liver and abdominal tissue samples were tested. Tissue samples (previously frozen) were procured just slightly over a 24-hour period postmortem. We precondition tissues samples as described in research literatures [Fung, 1993] to obtain consistent results. All samples were tested at room temperature $(21^0C \pm 3^0C)$.

Three indentation depths were applied with 5 mm (testing data-1), 10 mm (testing data-2) and 15 mm (testing data-3) to capture the force-displacement responses, respectively. Deformation examples were taken from a set of different surface points that were well distributed over surface of the sample tissues. In tissue relaxation

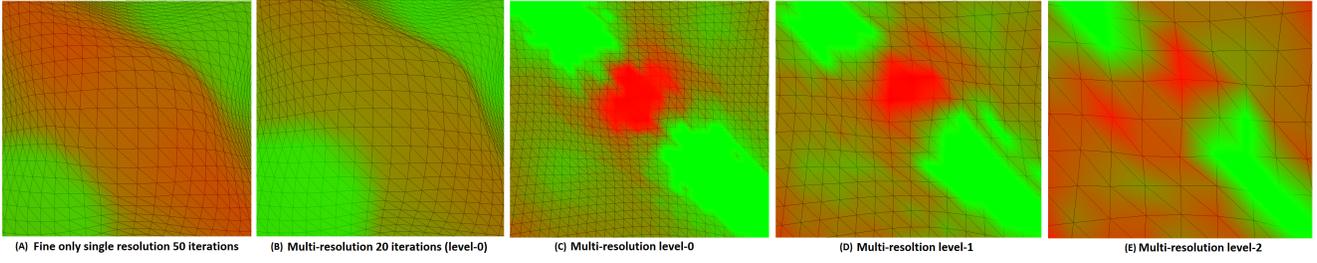| (A) Fine only single resolution 50 iterations | (B) Multi-resolution 20 iterations (level-0) | (C) Multi-resolution level-0 | (D) Multi-resoltion level-1 | (E) Multi-resolution level-2 |

Fig. 4. Strain distributions shown in colour map on a soft tissue (red colour indicates large strains and green colour indicates small strains). Images (A) and (B) show on the finest mesh level, where using a single mesh resolution requires a large number of iterations compared with a multi-resolution with only 20 iterations. Images (C), (D) and (E) show a three-level multi-resolution hierarchy strain distributions, the finer the mesh is, there are less strains and the better material stiffness.

tests, a sample was indented to the pre-defined depths in separate trials, then the indenter was kept in place until the tissue was fully relaxed. For stretch tests, the skin tissue was stretched along each of the biaxial directions to a pre-defined stretch length.

4 RESULTS AND DISCUSSION

4.1 Material parameters

In the context of medical simulations, the finite element model with the modified Neo-Hookean material is shown in Eq.3. It is still a challenging problem to obtain material properties as Young's modulus and Poission ratio. In this paper the elasticity parameter estimations is carried out as an inverse problem by minimizing the quadratic norm of the difference between the measured displacements obtained with the data acquisition system and the displacements resulted from the simulation model [Eskandari, et al., 2011]. The recovered Young's modulus and Poisson ratio through an off-line optimization program are then used in the multi-resolution strain limiting simulations.

4.1.1 Inverse problem

Assuming soft tissues are roughly incompressible isotropic homogeneous materials can significantly reduce the number of elasticity parameters [Park, 2006]. Furthermore, according to [Fung, 1993], Poisson ratio of soft tissues is selected in the range of $0.35 < \nu < 0.45$. During an optimization process, if the value of Poisson ration is fixed, it leaves Youngs modulus as the only unknown.

After applying finite element method, Eq. 7 describes the external force f and displacement u for all the nodes:

$$\mathbf{Ku} = \mathbf{f}, \tag{7}$$

where $\mathbf{K}$ is the stiffness matrix, which depends on the elasticity parameters (Young's modulus and Poisson ratio and the geometry of the elements; $\mathbf{f}$ is a vector of external forces. For a 3D object with N nodes, $\mathbf{K}$ is a $3N \times 3N$ matrix. The soft tissue material parameters needed in the simulator are $p = [E, \nu]$, where E is Young's modulus and ν is Poisson ratio. For a set of given indentation forces, displacements of a group points on tested tissue

samples and the simulated soft tissues are recorded. The objective function to be minimized is defined as the difference between the displacements $u^r(p)$ in the sample tissue and the displacements $u^s(p)$ in simulated tissue at the corresponding locations:

$$\mathbf{\Phi(p)} = \frac{1}{2} \sum \|\mathbf{u^s(p)} - \mathbf{u^r(p)}\|^2, \tag{8}$$

The parameter $p = [E, \nu]$ is iteratively updated using a descent algorithm. We employ the L-BFGS method based on the numerical analysis library ALGLIB [Alglib] to minimize the above objective function. At the $k - th$ iteration, a descent direction Δp_k is computed based on the gradient of Φ, and we search for an optimal step size λ along the direction based on the value and slop of the function:

$$\mathbf{\Phi(\lambda)} = \mathbf{\Phi(p_k + \lambda \Delta p_k)}, \tag{9}$$

where p_k is the vector containing the current estimate of the elasticity parameters. The gradient of the objective function is given by the chain rule:

$$\nabla \mathbf{\Phi(p)} = \sum \mathbf{J^T D} \|\mathbf{u^s(p)} - \mathbf{u^r(p)}\|, \tag{10}$$

where J is the Jacobian matrix of $u(p)$ and D is a matrix with each row essentially the spatial derivative of $\|u^s(p) - u^r(p)\|$ with respect to the $j - th$ axis. By differentiating both sides of Eq. 7, the derivatives of u with respect to the elasticities can be computed:

$$\left[\frac{\partial \mathbf{K}}{\partial E_j} \right] \mathbf{u} + \mathbf{K} \left\{ \frac{\partial \mathbf{u}}{\partial E_j} \right\} = 0, \tag{11}$$

Therefore, the Jacobian matrix for Young's modulus can be computed by solving Eq. 11 for each column J_j, $\mathbf{K} \left\{ \frac{\partial \mathbf{u}}{\partial E_j} \right\} = \left[\frac{\partial \mathbf{K}}{\partial E_j} \right] \mathbf{u}$, similarly, solving for the Jacobian matrix for Poisson ratio. The L-BFGS optimization algorithm uses the history of the gradient in previous steps to estimate the curvature and compute a symmetric positive definite approximation of the Hessian matrix [Nocedal, 1999]. Therefore, we do not need to supply the Hessian to the optimizer. To accelerate the optimisation process, while optimizing Young's modulus, Poisson ratio is kept constant for a number

of steps, then using the resulting Young's modulus to optimise Poisson ratio for a number of steps, and so on.

4.1.2 Parameter estimation

Initial values of elasticity parameters for optimisation are chosen based on common values used in medical simulation, for Youn's modulus within the range $10\ kPa < E < 60\ kPa$ and Poisson ratio between $0.3 < \nu < 0.45$. Table 1 lists initial material parameters and the estimated parameter values through optimisation.

TABLE 1
Estimation of Elasticities

Parameter	Initial	Iterations	Estimate
Porcine-liver			
E (kPa)	15	1500	16.36
ν	0.45	1500	0.44
Porcine-abdominal			
E (kPa)	30	2000	32.15
ν	0.40	2000	0.43
Skin-pad			
E (kPa)	50	1500	47.75
ν	0.45	1500	0.46

Fixed number of iterations is used in optimization process for parameter examinations. The optimization is an offline process. The elasticity parameters resulting from the optimization are then used in the multi-resolution strain limiting simulations.

4.2 Simulation of soft tissue

We developed a simulation system in C++ using OpenGL graphics API. The multi-core architecture of CPUs offers opportunities to the parallelization of physics computations. In our implementation, the SVD (single value decomposition) computation for each tetrahedron element is parallel computed with multi-threading operations. A mesh data set is designed into tetrahedral batches which are dedicated to a list of threads by the multi-threading component. Since a node can belong to several tetrahedron elements, care must be taken to ensure the memory of same variables is not accessed by different threads at the same time, otherwise the result will be undefined. The approach taken in our system implementation is not to update the forces directly on the nodes soon after the thread finishing, but to write its value into a temporary buffer that duplicates the shared nodes. This buffer is then accessed after the parallel pass so that each node is updated safely.

Figure 6 shows the results of computational time in milliseconds with respect to the number of CPU cores used and the number of tetrahedra, demonstrating an overall speed up in parallel computing SVD operations. It is worth noting that the speedup using multi-cores in parallel computing is limited by the time needed for the sequential fraction of the program where threads for one
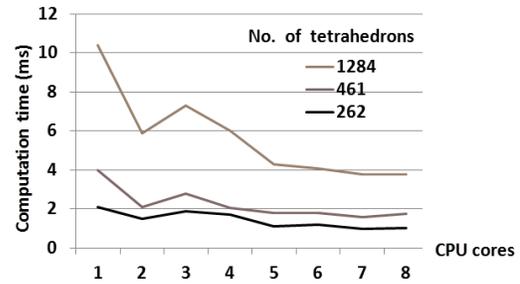

Fig. 6. Computational time with respect to CPU cores used and the number of tetrahedra computed.

step in the algorithm have to wait for the threads of the previous step to signal that they are ready. Although the synchronization and reconstruction processes introduce slight computation overhead as seen in figure 6 where the cost of synchronization outweighs the benefit of parallel when using 3 CPU cores than 2 cores, it is not a problem because the overall performance gain is definitely noticeable.

Tests were carried out in a single processor 8-core 3.40GHz Intel Xeon CPU with 16 GB RAM. Euler integration scheme was employed with step lengths chosen between 0.001 to 0.004 shown in table 1. Figure 7 shows computational speed up by using multi-resolution approach. Figure 7 shows computation times on a multi-resolution hierarchy with 3200 elements at the level-0, and 1800, 800 and 200 elements at levels 1, 2 and 3, respectively. A single mesh with 3200 elements and 200 constrained iterations requires an average of 40 milliseconds computation time, whereas a multi-resolution 4-levels approach requires an average of 11 milliseconds for a total of 200 iterations (50 iterations on each level). The significant speed up demonstrates that the multi-resolution approach can quickly archive convergence, because only 50 iterations are applied to the most dense mesh with 3200 elements. The subsequent meshes in the hierarchy each has far fewer constraints that can be enforced with 50 iterations. As can be seen in figure 7, the same multi-resolution hierarchy with 20 iterations on each level archives an interactive 6 milliseconds computational time, whereas table 2 demonstrates much higher numbers of tetrahedrons and iterations.

TABLE 2
Time and simulation performance

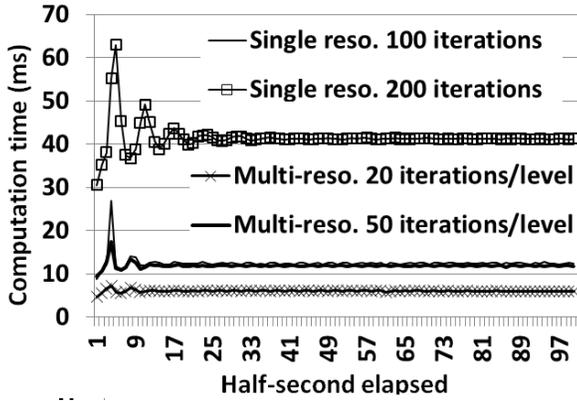|	Porcine-liver	Porcine-abdominal	Skin-pad
No. tets $H^{(0)}$	17.1K	16.4K	11.6K
levels	4	4	4
Time/frame	8.45s	7.0s	6.58s
Step length	0.004	0.004	0.001
λ_{max}	1.59	1.5	1.5
E(kPa)	16.36	32.15	47.75
ν	0.44	0.43	0.46
Iterations	155	165	125

Figure 8 shows comparisons between *ex vivo* samples

Fig. 7. Computational time comparison of single and multi-resolution simulations: single resolution has 3200 elements; multi-resolution has 4-levels with 3200 elements (level-0), 1800 elements (level-1), 800 elements (level-2) and 200 elements (level-3).
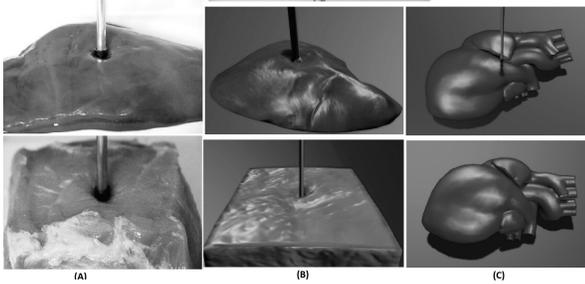

Fig. 8. Comparisons between sample tissues (A) and simulated soft tissues (B), and a simulated heart example (C).

and simulated soft tissues using the multi-resolution finite element algorithm. Parameters used for simulations are listed in table 2. Images in column (C) show a simulated heart with parameters $E = 50.0kPa, \nu = 0.45, \lambda_{max} = 1.20$.

4.3 Validation of force and displacement relationship

We defined a set of corresponding points both in the sample tissue and the simulated models, for which force and displacement measurements were taken at these locations to validate the proposed multi-resolution nonlinear simulation algorithm. Two *ex vivo* porcine tissues were tested in indentation tests, which were a size of $8 \ cm^3$ abdominal tissue *porcine-abdominal* and a *porcine-liver* tissue. A suturing skin pad *skin-pad* of size $8 \ cm \times 12 \ cm \times 2 \ cm$ was also used in indentation tests, which was considered as is an ideal testing media for iso-tropic soft tissue materials. Nonlinear material properties of these samples were evaluated as *force-displacement* relationships as shown in Figure 9 for indentation tests of simulation and tissue samples.

Tissue relaxation tests evaluate the material behavior in terms of the force-time relationship to show the material nonlinearity after an indentation force being released. Figure 9(D) compares relaxation behaviors of the simulated data and tested tissue samples after 10

mm indentation depth. The close match between the two demonstrates the capability of the proposed constrained finite element algorithm can effectively capture soft tissues' material properties.

4.4 Force and stretch ratio

Stretch tests are designed to measure force-deformation responses along two biaxial directions to show material nonlinear characteristics. Literature [Fung, 1993] and [Brouwer et al., 2001] show that the material nonlinearity can be expressed as an exponential function given by the *force-stretch ratio* relationship: $\|\mathbf{f}(\lambda)\| = \gamma e^{\alpha\lambda}, \frac{d\mathbf{f}}{d\lambda} = \alpha\mathbf{f}, \lambda = \frac{l}{l_0}$, where $\mathbf{f}(\lambda)$ is the measured force, l and l_0 are the stretched and the rest tissue length, respectively. α and γ are coefficients of tissue stiffness which can be found through curve-fittings. Taking the derivative $\frac{d\mathbf{f}(\lambda)}{d\lambda}$, the stress due to stretching along two biaxial directions is dependent on stretching ratio λ. In our stretch tests, λ is the (applied) stretch in the principal directions in Eq. 2.

Stretch tests were carried out on a $8 \ cm^2$ square skin sample using the experimental setup shown in figure 5. Triangle meshes were used in our simulation for modelling the skin deformation using the proposed multi-resolution algorithm. We build a 2×2 deformation matrix from $\mathbf{d_x}$ and $\mathbf{d_X}$, where $\mathbf{x}$ is the current position and $\mathbf{X}$ the reference position of a vertex. Thus, we compute two dimensional strain-limiting along the two principal stretch directions using triangular elements. Figure 10 (A) and (B) compare the simulation data with the testing data, which demonstrate the nonlinear biphasic behavior of skin tissue under stretch forces with highly stiff incompliant material behaviors. Figure 10 (C) captures nonlinear characteristics of the skin and shows a simulation example of the proposed algorithm on a three-level multi-resolution hierarchy, and simulation parameters were $E = 180, \nu = 0.45$.

5 CONCLUSION AND FUTURE WORK

We present a novel strain based constraint finite element method for simulating nonlinear homogeneous soft tissues efficiently. The algorithm is capable of modeling rich nonlinear deformations in a straightforward finite element framework. The proposed algorithm achieves an average of 11 milliseconds computational time interactive frame rate on a 4-level multi-resolution hierarchy with 50 constrained iterations on each level, a 70 percent speed up compared with a single level with the same total number of iterations. Therefore, the algorithm offers effective simulations for nonlinear soft tissue properties with highly incompliant material characteristics. Simulation results were validated by experimental data captured by a simple-to-build system. Measurements on *ex vivo* soft tissues were taken and compared with simulation data. We would like to implement a virtual reality suturing application for
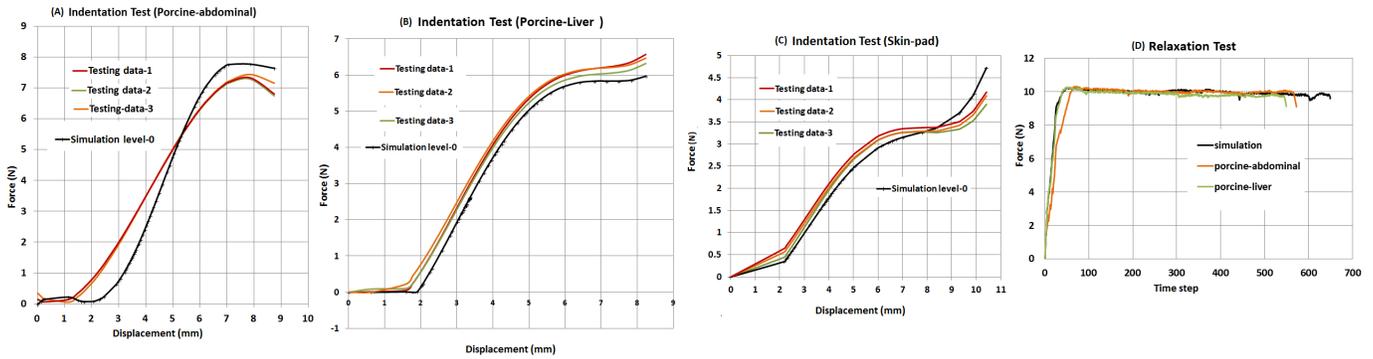
Fig. 9.   (A), (B)and(C): Force-displacement measurements taken from *ex vivo* porcine-abdominal, porcine-liver, and skin-pad tissues and simulation data. (D): comparisons the relaxation processes between simulated and experiment tissues for 10 mm indentation depth.
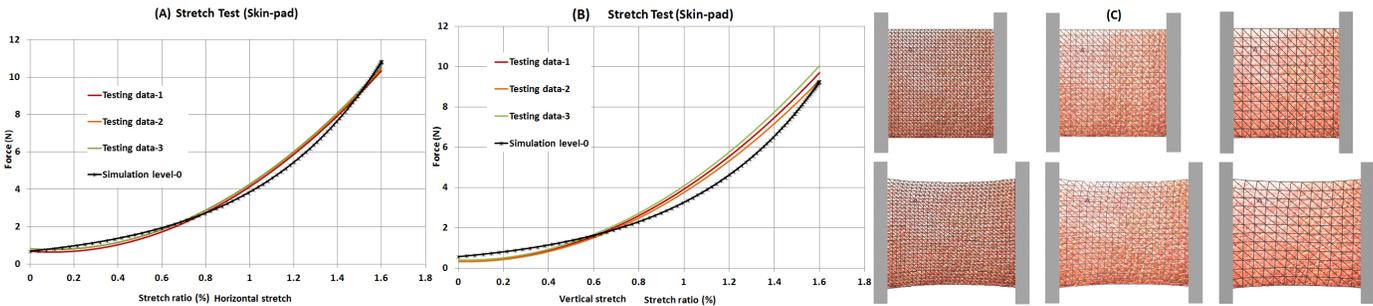

Fig. 10. (A) and (B): A stretching experiment compares stretching strain-force responses between simulated and skin-pad sample; (C): A simulation example of horizontal stretch of simulated skin using three levels of multi-resolution triangle elements with 2048, 968 and 338 triangle elements at level 0, 1 and 2, respectively.

which the proposed algorithm is applicable in terms of isotropic and incompliant material behaviors.

We aim to improve our tests in the future work including the selection of tissue samples, i.e tissues that are mixed with glandular and fibrous materials such as kidney. These soft tissues will challenge the current assumptions of isotropic material behavior and anisotropic materials will need to be addressed in our future work. It is also worth exploring to what extent the proposed approach could capture anisotropy by using different stretch ratios with respect to each principal directions.

REFERENCES

[Alglib]   *http://www.alglib.net/.*
[Beer et al., 1981] Beer F. P and Johnston E. R., Jr.:   *Mechanics of materials.* New York: McGraw-Hill, 1981
[Bickel et al., 2009] Bickel B., Baecher M., Otaduy M. A., Matusik W., Pfister H., and Gross M.: *Capture and modeling of non-linear heterogeneous soft tissue.* Proc. of ACM SIGGRAPH, 28(3):10811094, 2009.
[Bonet and Wood, 2008] Bonet J., Wood R. D.: *Nonlinear continuum mechanics for finite element analysis.* (2nd edition). Cambridge University Press. Cambridge, UK; New York, NY, USA, 2008.
[Brouwer et al., 2001] Brouwer I., Ustin J., Bentley L., Sherman A., Dhruv N.,and Tendick F.: *Measuring in vivo animal soft tissue properties for haptic modeling in surgical simulation.* Medicine Meets Virtual Reality 2001, pp. 69-74, 2001.
[Chentanez et al., 2009] Chentanez N., Alterovitz R. , Ritchie D., Cho L., Hauser K. K., Goldberg K., Shewchuk J. R., and O'Brien J. F.: *Interactive simulation of surgical needle insertion and steering.* In Proceedings of ACM SIGGRAPH 2009, pp. 88:110, Aug 2009.

[Demmel, 1997] Demmel J.: *Applied numerical linear algebra.* SIAM, Philidelphia, PA 1997.
[Eskandari, et al., 2011] Eskandari, H., Salcudean, S. E., Rohling, R., and Bell, I.: *Real-time solution of the the finite element inverse problem of viscoelasticity.* Inverse Problems, vol. 27, No. 8:085002.
[Fung, 1993] Fung.Y. C.: *Biomechanics: mechanical properties of living tissue.*Second ed. Springer-Verlag, New York, 1993.
[Gefen and Margulies, 2004] Gefen A., Margulies S.S.: *Are in vivo and in situ brain tissues mechanically similar?* Journal of Biomechanics, Vol 37, pp 1339-1352, 2004.
[Gimas]   *http://www.gimias.net/.*
[Holzapfel, 2004] Holzapfel G. A.: *Nonlinear solid mechanics: a continuum approach for engineering.* John Wiley and Sons, Ltd. 2004.
[Humprey, 2003] Humphrey J. D.: *Continuum biomechanics of soft biological tissues* in Proceedings of the Royal Society of London. A, 459, pp 3-46, 2003.
[Irving et al., 2006] Irving G., Teran J., and Fedkiw R.: *Tetrahedral and hexahedral invertible finite elements.* Graph. Models, 68(2), pp 6689, 2006.
[James and Pai, 2002] James D. and Pai D.: *DyRT: Dynamic response textures for real time deformation simulation with graphics hardware.* ACM Trans. Graph. (SIGGRAPH Proc.), 21, 2002.
[Krouskop et al., 1998] Krouskop T.A., Wheeler, T.M., Kallel, F., Garra, B.S.Hall, T.: *Elastic moduli of breast and prostate tissues under compression.* Ultrasonic Imaging, 20, 260-274, (1998).
[Lee and Radok, 1960] Lee E. H. and Radok J. M.: *The contact problem for viscoelastic bodies.* J. of Applied Mach. 27, pp 438-444, 1960.
[Mendis, 1995] Mendis K. K. , Stalnaker R. L., and Advani S. H.: *A constitutive relationship for large deformation finite element modeling of brain tissue.* Journal of Biomechanical Engineering, 117, pp. 279-285, 1995.
[Müller et al., 2001] Müller M., McMillan L., Dorsey J., and Jagnow R.: *Real-time simulation of deformation and fracture of stiff materials.* In Comput. Anim. and Sim. '01, Proc. Eurographics Workshop, pages 99.111. Eurographics Assoc., 2001.
[Müller, 2008] Müller M.: *Hierarchical position based dynamics.* In Proc. of Virtual Reality Interactions and Physical Simulations, 2008.

[Ogden, 1997] Ogden R. W.: *Nonlinear Elastic Deformations*. Courier Dover Publications, 1997.

[Park, 2006] Park E. and Maniatty A. M.: *Shear modulus reconstruction in dynamic elastography:time harmonic case*. Phys. Med.Biol. vol(51) 3697-721, 2006.

[Nocedal, 1999] Nocedal J. and Wright S. J.: *Numerical optimization*, Springer, 1999.

[Pratt et al., 2010] Pratt P., Stoyanov D. , Visentini-Scarzanella M., and Yang G-Z.: *Dynamic guidance for robotic surgery using image-constrained biomechanical models*. MICCAI 2010 Proceedings of the 13th international conference on Medical image computing and computer-assisted intervention: Part I, pp. 77-85, 2010.

[Samur et al., 2007] Samur E., Sedef M., Basdogan C., Avtan L., and Duzgun O.: *A robotic indenter for minimally invasive measurement and characterization of soft tissue response*. Medical Image Analysis. Vol. 11(4), pp. 361-73, 2007.

[Si, 2010] *http://tetgen.berlios.de/*

[Taylor et al., 2008] Taylor Z. Cheng M, and Ourselin S.: *High-speed nonlinear finite element analysis for surgical simulation using graphics processing units*. IEEE Trans. Med. Imag., vol. 27, no.5, pp. 650-663, 2008.

[Tang et al, 2012] Tang W., Wan R T., Gould D., How T., and John W N.: *A Real-time nonlinear elastic approach to simulating guide-wire and catheter insertions based on cosserat rod*. IEEE Transactions on Biomedical Engineering, vol 59, No. 8, pp.2211- 2218, 2012.

[Vidal et al., 2012] Vidal P. F., Villard P-F., Lutton É. : *Tuning of patient-specific deformable models using an adaptive evolutionary optimization strategy*. IEEE Transactions on Biomedical Engineering, vol. 59, No. 10, October 2012.

[Wang et al., 2010] Wang H., O'Brien J. F., Ramamoorthi R.: *Multi-resolution isotropic strain limiting*. ACM Trans. Graph. vol. 29(6): pp.156:1-156:10, 2010.

PLACE PHOTO HERE

Wen Tang received her PhD degree in Engineering and Computer Science from University of Leeds, UK. She is currently an Associate Professor in the School of Computing at the University of Teesside, UK. He research interests are in physically-based computer simulation algorithms, data-driven analysis and interactive techniques for applications in medicine.

PLACE PHOTO HERE

Tao Ruan Wan received his PhD degree in Engineering and Computer Science from University of Leeds, UK. He is now working in the School of Creative Technology at the University of Bradford, UK as a Senior Lecturer. His research interests are in the area of virtual reality simulation and modelling, including medical image analysis, surgical simulation, interactive technologies in human-computer interactions and haptic interfaces.